journal

J. Am. Ceram. Soc., 1–8 (2016)
DOI: 10.1111/jace.14148

Mullite–Nickel Magnetic Nanocomposite Fibers Obtained from Electrospinning Followed by Thermal Reduction

Zhaoxi Chen,[‡] Yu Gu,[‡] Pavel Aprelev,[‡] Konstantin Kornev,[‡] Igor Luzinov,[‡] Jie Chen,[§] and Fei Peng[‡,†]

[‡]Department of Materials Science and Engineering, Clemson University, Clemson, South Carolina

[§]School of Physics and Electrical Technology, Yancheng Teachers University, Yancheng, Jiangsu

Mullite–nickel nanocomposite fibers with Ni nanoparticles of controllable size, dispersion, and consequent magnetic properties were fabricated using sol–gel/electrospinning method, followed by thermal reduction. The fibers were electrospun from an aqueous solution containing sol–gel mullite precursor and nickel nitrate. These fibers were then heat treated in the reducing atmosphere between 550°C and 750°C to achieve fine-dispersed metallic Ni nanoparticles (NPs). After the Ni^{2+} was reduced to Ni NPs at 750°C for 10 h, the fibers were then directly transformed to the mullite fibers at 1000°C without the undesirable intermediate spinel phase. In many high-temperature applications, mullite is the desired phase than spinel. If not fully reduced, the Ni^{2+} cations induce early precipitation of spinel phase before mullite can be formed. This spinel phase was a solid solution between Al_2NiO_4 and Al-Si spinels, which later reacted with the residual silica and formed a mixture of mullite and spinel at 1400°C. The formation of spinel phase was suppressed or fully eliminated with chemically reducing Ni^{2+} to metal NPs. The average size of nickel NPs within the fibers was ~20 nm, insensitive of the Ni concentration and reducing temperature. However, the Ni NPs on the fiber surface grew as large as ~80 nm due to fast surface diffusion. The magnetic nanocomposites exhibited ferromagnetism with saturation magnetization (M_s) close to pure nickel of the same nominal weight, but coercivity (H_c) much smaller than the bulk nickel, indicating the nature of bimodal magnetic nanoparticle distributions. The majority of small Ni NPs (~20 nm) within the fibers exhibited superparamagnetism, while the minor portion of relatively large NPs (50–80 nm) showed ferromagnetism.

I. Introduction

Many research efforts have been made to fabricate nanocomposites with unique properties and multifunctionality enabled by the nanoscale microstructure.[1–5] Novel properties have been achieved with the ceramic-based nanocomposites of embedded metallic nanoparticles (NPs). Especially in the recent years, fabricating such nanocomposites has been a growing field of materials science.[3–6] Controlling the dispersion and the size distribution of the NPs is the key to achieve optimum performance and desired properties.[7] These nanocomposites can be achieved using thermal reduction, mechanical mixing, liquid phase deposition, chemical vapor deposition, laser deposition, or sol–gel method.[8–20] The thermal reduction method is one of most commonly used ones, through which metal oxide precursors can be converted to dispersed metallic nanoparticles with a heat treatment in the reducing atmosphere.[5,8,21–23] Aerogels, films, fibers, and powders are especially suitable for this method due to their low density, open porous structure, and high specific surface area that allow easy diffusion of reducing gases.[5,8,24–26]

Transition-metal NPs often have interesting properties and important applications in catalysts, sensors, magnetic, electronic, and optical devices.[25] Nickel NPs are particularly important as catalytic, conductive, and magnetic materials. Embedding Ni NPs into the ceramic matrix provides the magnetic functionality, which can be used for nondestructive evaluation of the materials condition.[27] The SiO_2/Ni, Al_2O_3/Ni, TiO_2/Ni, Y-TZP/Ni, and ZrO_2/Ni ceramic/metal nanocomposites have been studied extensively.[2,4,5,25,28–30] The thermal reduction method is one of the most convenient ways to introduce dispersed nickel NPs.[4,5,28–30] Reduction sintering of ceramics with additives of NiO or Ni^{2+} salts resulted in intragranular Ni NPs of sizes between 20 and 100 nm dispersed at the grain boundaries and within the grains of an oxide host.[4,5,29]

Mullite ($3Al_2O_3{\cdot}2SiO_2$) fibers have excellent high-temperature strength, creep resistance, and chemical stability.[31–34] Thus they have been widely used as the reinforcement in the ceramic matrix composites.[35,36] These fibers can also be used as the high-temperature thermal or electrical insulating materials.[36,37] Electrospinning is a versatile processing technique for ceramic fibers, especially nanofibers.[38–40] In our previous study, mullite fibers have been successfully fabricated using electrospinning.[40] Controlling the precursor rheology and spinning conditions, we obtained mullite fibers with relatively uniform microstructure and narrow diameter distributions.[40] We showed that high-molecular weight polyethylene oxide (PEO) helped to improve the controllability of fiber spinning.[40]

In this work, we present the method of synthesizing mullite–nickel nanocomposite fibers using electrospinning, followed by thermal reduction. Intermediate phases such as the spinel phase can be avoided with proper heat-treatment procedures. We found that the Ni NPs within the mullite fiber has an equilibrium size of ~20 nm, while the Ni NPs on the fiber surface can grow much larger. The magnetic properties of the nanocomposite fibers reflect this microstructure feature.

II. Experimental Procedure

(1) Fabrication of Mullite Fibers with Embedded Ni NPs

Preparation of mullite fibers using electrospinning was similar to our previous work, in which pure mullite fibers were fabricated.[40] In this study, nickel nitrate was used as the Ni source in the precursor. Aluminum isopropoxide [AIP; Al

P. Joy—contributing editor

Manuscript No. 36876. Received May 15, 2015; approved January 2, 2016.
[†]Author to whom correspondence should be addressed. e-mail: fpeng@clemson.edu

$(C_3H_7O)_3$, 98%, Alfa Aesar, Ward Hill, MA], aluminum nitrate (AN, $Al(NO_3)_3{\cdot}9H_2O$, 98%, Alfa Aesar), tetraethyl orthosilicate [TEOS, $Si(OC_2H_5)_4$, 98%, Acros Organics, NJ], and nickel nitrate hexahydrates [$Ni(NO_3)_2{\cdot}6H_2O$, 95%, Aldrich, St. Louis, MO] were used to synthesize the precursor. Water was used as the solvent. The molar ratio between each component was AIP:AN:TEOS = 11:4:5. The AN was dissolved in deionized water at room temperature by vigorously stirring for 30 min. Then AIP and TEOS were added into the solution and stirred for 20 h. The AIP and TEOS were dissolved completely, and clear solutions were obtained. The obtained solution was then refluxed at 80°C for 5 h. Approximately 2/3 part of the solvent was removed using a rotary evaporator (IKA RV 10 digital; IKA Works, Inc., Wilmington, NC). The obtained solutions were then set in an oven at 80°C until viscous sols were formed. The spinnability of these sols was determined using hand drawing with a glass rod. A PEO (MW 1 000 000, Aldrich) solution of 2 wt% in H_2O was prepared separately as the spinning aid solutions. The precursor sol was diluted in ethanol and mixed with nickel nitrate at varying concentrations (0, 2, 5, and 10 wt% of mullite yield). The volume ratio between precursor sol, ethanol, and PEO solution was fixed at 4:8:1. The fibers were electrospun under an applied electrical field generated using a high-voltage supply (Model PS/FC60P02.0-11; Glassman High Voltage Inc., High Bridge, NJ). A positive voltage of 10 kV was applied to the needle of the syringe containing e-spun solutions driven by a syringe pump (Model NE-300; New Era Pump System Inc., Farmingdale, NY). The flow rate was set to approximately 0.5 mL/h. The needle was placed 20 cm aside from the collector. The fibers were produced at 25%–35% ambient relative humidity and collected using a rotating collector. The rotating collector has four grounded stainless steel bars, with a gap of ~5 cm between each pair of adjacent bars. The fibers were then cut from the collector and collected in the form of mats. The obtained fibers were dried at 60°C for 24 h before heating.

In order to obtain the mullite phase with embedded nickel NPs, a two-step heating sequence was applied. In the first step, the precursor fibers were heat treated in the reducing gas (5 vol% H_2 in Ar) to a designed temperature between 650°C and 750°C and isothermally kept for 10 h to form metallic NPs. The heating rate was set at 1°C/min below 500°C and 5°C/min above 500°C. In the second step, the fibers were heat treated and crystallized at 1000°C for 30 min under 5% H_2-Ar. Table I summarizes detailed information for samples named with different nickel concentration and heat-treatment conditions.

(2) Characterization

The thermal behaviors were studied at different heating rate under flowing air or 5% hydrogen-argon condition using DTA (DTA7; Perkin Elmer, Waltham, MA). The crystalline phases were identified using X-ray diffraction (XRD; Rigaku Co., Ltd., Tokyo, Japan); the microstructure was characterized using scanning electron microscopy (SEM, Hitachi S4800, Hitachi, Ltd., Tokyo, Japan) and transmission electron microscopy (TEM, Hitachi 9500 300 kV microscope, Hitachi, Ltd.). The average size of fiber diameters or Ni NPs on the fiber surface was calculated from the average of more than 100 randomly selected fibers or NPs taken from SEM micrographs. The magnetic properties of the composite fibers were measured by using the Alternating Gradient Magnetometer (AGM 2900; Princeton Measurements, Inc., Princeton, NJ).

III. Results

(1) Precursor Decomposition and Phase Identification

With increasing nickel concentration, the solution gradually changed from light green to dark green while remaining transparent. The fiber mats with 5 wt% Ni were dark gray after reduction, indicating the formation of metallic phase. The fibers that were heat treated in air showed a white-bluish color.

Figure 1 shows the XRD traces of mullite–nickel fibers after heat treatment in 5% hydrogen. The detailed heat-treatment procedure for each sample code is given in Table I. The near complete conversion of Ni^{2+} to Ni was reached after thermal reduction at 750°C for 10 h. For all five samples (MN2-750R-1000, MN5-750R, MN5-750R-850, MN5-750R-1000, and MN10-750R-1000), mullite and nickel were the only two phases observed after the sample was first reduced at 750°C and then quenched at 850°C or crystallized at 1000°C. No residual NiO or spinel phase was observed. Mullite peaks of MN5-750R and MN5-750R-850 were weak. The mullite peaks became strong for MN5-750R-1000. The intensities of nickel peaks compared to the peaks of mullite

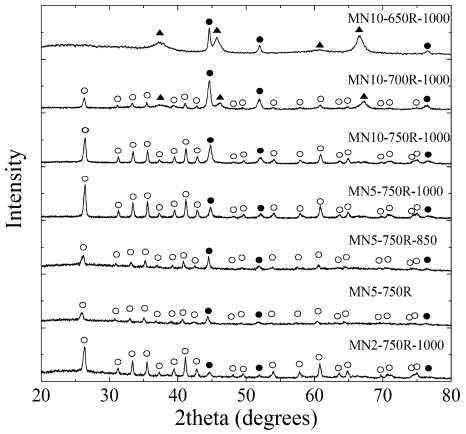

Fig. 1. XRD patterns of mullite–nickel nanocomposite fibers with different Ni concentration heat treated in 5% H_2-Ar for 10 h, and/or then heated at 850°C or 1000°C for 30 min. Labeled phases: ● nickel, ○ mullite, ▲ spinel.

Table I. Materials Composition, Isothermal Reduction Temperature, and Heat Treatment Atmosphere for Different Ni–Mullite Fibers

Specimen codes	Nickel content (wt%)	Isothermal reduction temperature (10 h)	Crystallization temperature	Heat treatment atmosphere
MN0-A	0	NA	Quench between 1000°C and 1400°C	Air
MN2-750R-1000	2	750°C	1000°C for 30 min	5 at.% H_2 in Argon
MN5-750R-1000	5	750°C	1000°C for 30 min	5 at.% H_2 in Argon
MN5-750R	5	750°C	NA	5 at.% H_2 in Argon
MN5-750R-850	5	750°C	Quench at 850°C	5 at. % H_2 in Argon
MN5-A	5	NA	Quench between 1000°C and 1400°C	Air
MN5-H_2	5	NA	Quench between 1000°C and 1400°C	5 at. % H_2 in Argon
MN10-750R-1000	10	750°C	1000°C for 30 min	5 at. % H_2 in Argon
MN10-700R-1000	10	700°C	1000°C for 30 min	5 at.% H_2 in Argon
MN10-650R-1000	10	650°C	1000°C for 30 min	5 at.% H_2 in Argon

relatively enhanced with increasing nickel loading, as shown with samples MN2-750R-1000, MN5-750R-1000, and MN10-750R-1000. Coexistence of mullite, nickel, and spinel phase was observed in samples (MN10-700R-1000) that were reduced at 700°C for the same duration. The spinel phase was probably a solid solution between Ni-Al spinel (Al_2NiO_4) and Al-Si spinel (near $SiO_2{\cdot}6Al_2O_3$), which will be discussed in the Discussion part. Only nickel and spinel phase were observed in the sample that was reduced at 650°C and then heated to 1000°C (MN10-650R-1000).

The results of Fig. 1 suggest that the Ni^{2+} concentration influences the crystallization behavior of mullite. To study this effect, we carried out heat treatment on MN0A and MN5A samples in air from room temperature to 1400°C. The XRD patterns of the specimens after calcining at different temperatures are shown in Figs. 2 and 3. The fibers without Ni^{2+} addition (MN0-A) remained amorphous at low temperatures and were directly transformed to mullite after calcining at 1000°C. No intermediate phase, such as spinel was observed. In the fabrication of mullite using the sol–gel processing, elimination of the spinel phase was desired but challenging.[41–43] However, when 5% Ni^{2+} was doped, the spinel phase was observed in MN5-A fibers after calcining at 1000°C, 1100°C, 1200°C, and 1300°C. Trace amount of mullite was observed at temperatures between 1000°C and 1300°C. After calcined at 1400°C, the obtained phases were mullite and α-Al_2O_3.

The DTA scans of pure mullite and 5% Ni-doped mullite gels under air or 5% H_2 are shown in Fig. 4. The curves of MN0-A, MN5-H_2, and MN5-A are similar at low temperatures, as shown in Fig. 4(a). The endothermic peaks around 150°C and 300°C were due to loss of residual solvents and decomposition of organic components. Diverse DTA profiles were observed at temperature ranging from 900°C to 1000°C. MN0-A showed a sharp exothermic peak at around 980°C which was due to mullization (crystallization of mullite).[40] While a broad exothermic peak corresponding to mullization was observed in MN5-750R-H_2 at around 950°C. The observation of mullite phase in XRD at relatively low temperatures (i.e., 750°C for MN5-750R and MN5-750R-850 shown in Fig. 1) was possibly due to the long-time annealing. MN5-A showed a broad exothermic peak at around 930°C corresponding to the crystallization of Al-Si spinel. No endo- or exothermic peak at temperature ranging from 900°C to 1000°C was observed in MN5-H_2.

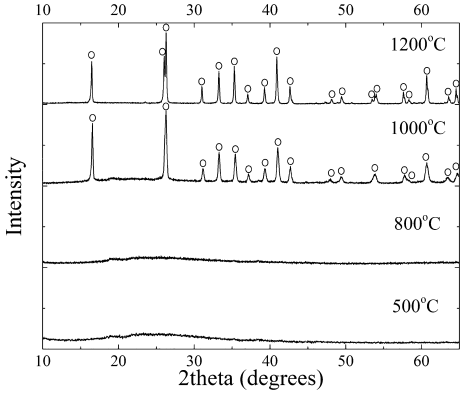

Fig. 2. XRD traces of pure mullite fibers heat treated in air. Labeled phases: ○ mullite.

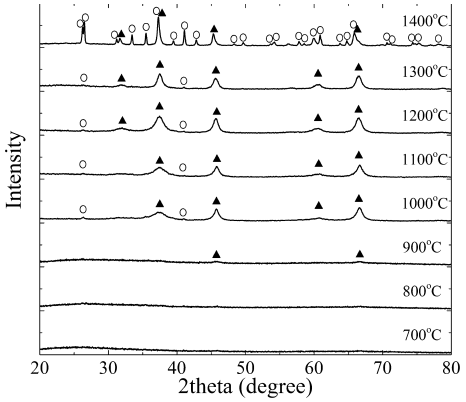

Fig. 3. XRD traces of MN5-A (5 wt% Ni loading) fibers heat treated in air. Labeled phases: ○ mullite, ▲ spinel.

(2) Materials Microstructure

(A) Fibers: Figure 5 shows the SEM micrographs of mullite–nickel fibers after heat treatment in hydrogen. The fiber showed uniform diameter and good straightness. Nickel particles were observed on the surface of the fibers. Diameters of 800 nm–1 μm were observed. A slight deviation in fiber diameters was also observed.

(B) Ni NPs: Figure 6 shows the TEM images of reduced mullite–nickel fibers with 2 and 5 wt% Ni doping. The TEM images indicate that the metallic phase NPs were dispersed within the mullite matrix. No separation at the boundary was observed between mullite and Ni phase which indicates good adhesion between the metal and ceramic phases.

The average sizes for Ni NPs observed from fiber surface using SEM micrographs are summarized in Table II. We observed generally smaller Ni NPs within the fiber than on those on the surfaces. However, using TEM, it was difficult to generate a representative average particle size. Thus, here we only present the particle sizes on the surface, which was obtained from SEM micrographs. In the ceramic/metal nanocomposites derived from reduction of solid solution, a bimodal particle size distribution for the dispersed phase was usually observed.[44] Relative large particles were observed on the surface of the fibers and small particles were embedded within the fiber matrix. The increasing of Ni loading gave rise to large size for Ni NPs and range of size distribution, which was ascribed to the increasing amount of metal phase and coalescence of the NPs on the surface.[5]

The electronic, magnetic, and catalytic properties of metal NPs strongly depend on the particle size.[45] The average crystallite size of nickel was determined by the Scherrer equation from the X-ray diffraction[46,47]:

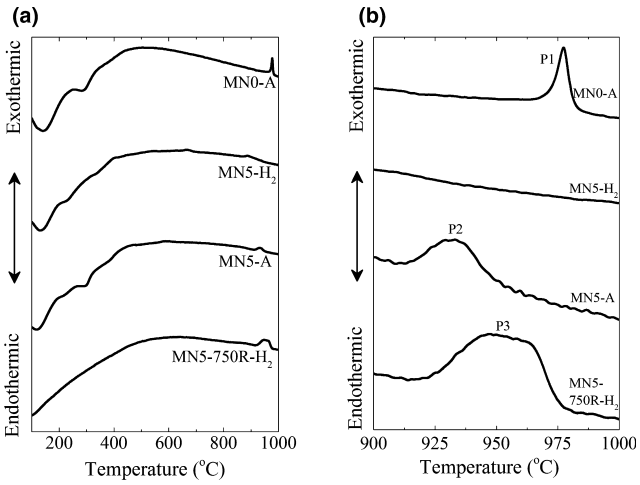

Fig. 4. Curves of DTA scans at 5°C/min for pure mullite gel in air (MN0-A), 5% Ni-mullite in 5% H_2 (MN5-H_2), 5% Ni-mullite in air (MN5-A), and 5% Ni-mullite preheat treated at 750°C for 10 h under 5% H_2 (MN5-750R-H_2). P1, P2, and P3 are the exothermic peaks between 900°C and 1000°C.

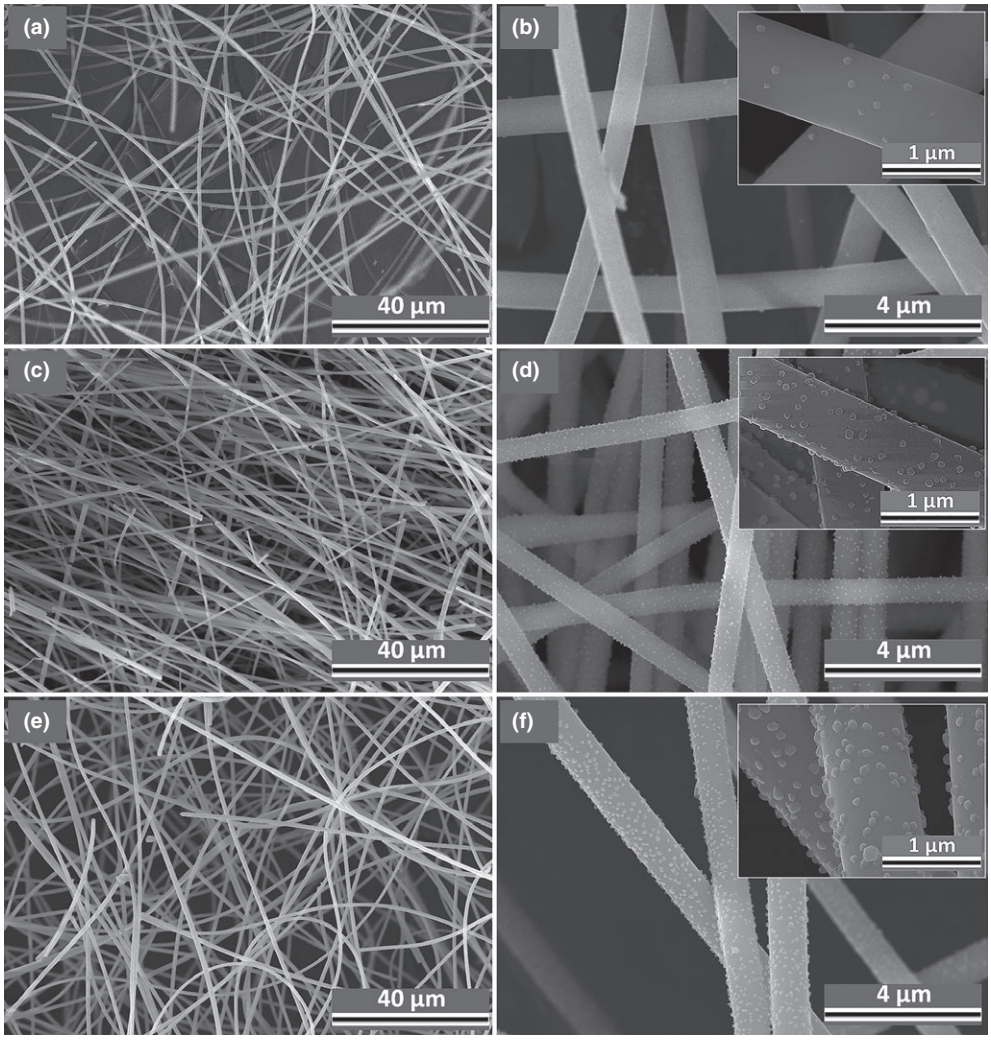

Fig. 5. SEM images of MN2-750R-1000 [(a) & (b)], MN5-750R-1000 [(c) & (d)], and MN10-750R-1000 [(e) & (f)] mullite–nickel nanocomposite fibers after the heat treatment specified in Table I.

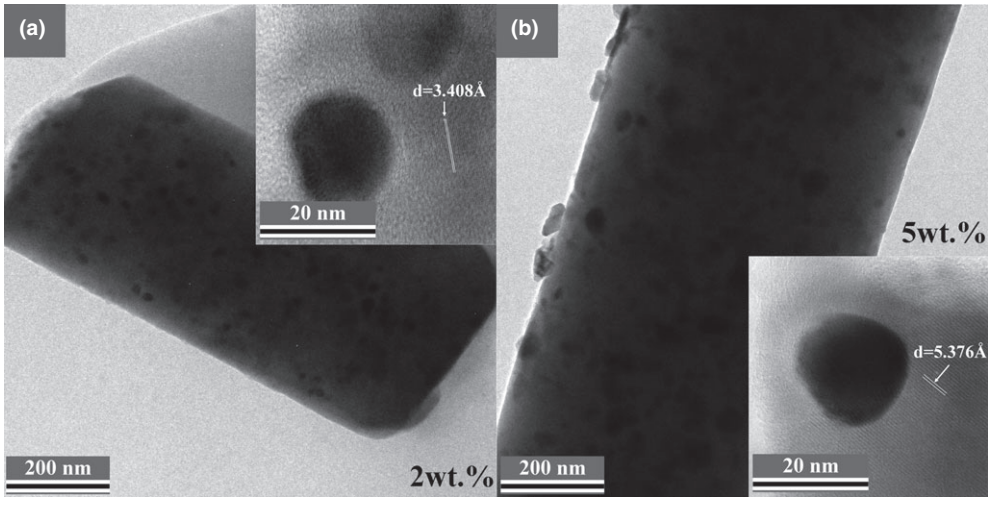

Fig. 6. TEM images of MN2-750R-1000 (a) and MN5-750R-1000 (b) specimen.

$$\tau = \frac{K_s \lambda}{\beta \cos\theta} \quad (1)$$

where τ is the crystallite size, K_s the dimensionless shape factor (equal to 0.9 for spherical crystallite), λ the wavelength of X-ray (1.54 Å used in our experiment), β the full width at half the maximum intensity (FWHM), and θ the X-ray diffraction angle. The τ values for MN2-750R-1000, MN5-750R-1000, and MN10-750R-1000 specimens were calculated according to Eq. (1) and is summarized in Table II. The values were obtained from the peaks corresponding with [111] plane which showed the highest intensity. The calculated τ of

Table II. Particle Size of Nickel and the Magnetic Properties

Specimen name	Average surface particle size (nm)	Overall average particle size (Å)	Saturation M_s (Am^2/kg)	Remanence M_r (Am^2/kg)	Coercivity H_c (kA/m)	Observed phase (s)
MN10-750R-1000	80	192	4.177	1.136	6.83	Mullite and Ni
MN10-700R-1000	75	NA	3.494	0.592	4.62	Mullite, spinel, and Ni
MN10-650R-1000	40	NA	0.199	0.031	2.47	Spinel and Ni
MN10-550R-1000	15	NA	0.085	0.005	1.68	Spinel and Ni
MN5-750R-1000	55	204	1.826	0.409	4.09	Mullite and Ni
MN2-750R-1000	25	185	0.918	0.091	1.74	Mullite and Ni

nickel had almost identical values of around 20 nm. The τ values were compared with the particle size evaluated from SEM and TEM. The particle size in MN2-750R-1000 specimen was very close to the τ value obtained, indicating single crystal character for the Ni NPs. While in higher Ni loaded samples, a significant greater particle size was observed on the fiber surface. As mentioned, the SEM and TEM studies indicate a bimodal size distribution of Ni NPs on the surface and within the fiber. The larger particle size was caused by the coalescence of Ni crystallites on the fiber surface, due to fast diffusion on the surface.

(3) Magnetic Properties

Nickel is one of the most important magnetic materials. The magnetic composite fibers could be attracted and lifted by a magnet. Figure 7 shows the magnetization versus magnetic field plots (M–H loop) of mullite–nickel composite fibers. Notable hysteresis was observed for 5% and 10% Ni loaded samples indicating ferromagnetism. The saturation magnetization M_s, remanence M_r, and coercivity H_c of the samples are summarized in Table II. The measured magnetic moments were normalized by the total weight of the composite fiber. The M_r and H_c values were determined by the zero magnetic moment and magnetic field. At 300 K, a small M_s was measured on MN10-550R-1000 and MN10-650R-1000 fibers. The M_s of MN10-700R-1000 was about 17 times of the MN10-650R-1000. The MN10-750R-1000 fibers exhibit highest M_s of 41.8 Am^2/kg and H_c of 6.83 kA/m. With the increasing temperature for thermal reduction, significant increase in M_s was observed, which implied a greater portion of Ni^{2+} cations were transformed into the metallic form. The H_c value increased with increasing Ni concentration and temperature for thermal reduction, which implied greater particle size of Ni.

IV. Discussion

(1) Phase Transformations with Different Heating Treatments

In many of the ceramic/Ni systems, the reduction of Ni^{2+} to the metallic form has been found the key to achieve desired microstructures and phases.[2,4,5,29] The thermal reduction of Ni^{2+} was usually performed in a crystalline matrix.[2,4,5] For instance, Sekino et al. reported the complete reduction of Ni^{2+} to nickel metal in α-Al_2O_3/NiO mixture by the heat treatment at 700°C.[5] Consider the equilibrium condition of $NiO_{(s)} + H_{2(g)} \rightleftharpoons Ni_{(s)} + H_2O_{(g)}$, the reaction constant is expressed as the partial pressure of the product, P_{H_2O} divided by the partial pressure of the reactant, P_{H_2}. We can relate the equilibrium constant (K) to the reaction Gibbs energy change at the standard state (ΔG^0) by[48]:

$$K = \exp\left(-\frac{\Delta G^0}{RT}\right) \tag{2}$$

where R is the gas constant and T the absolute temperature. In our case, before reduction, NiO was dissolved in the aluminosilicate amorphous matrix and formed a homogeneous solution without noteworthy phase separation.[49,50] If we assume that the solution is an ideal solution (for small NiO concentration, this assumption is a good approximation), the Gibbs energy change per mole due to forming this solution can be derived as[51]:

$$\Delta G_{mix} = -RT[x \ln x + (1-x)\ln(1-x)] \tag{3}$$

where x is the molar fraction of NiO in amorphous aluminoslicate glass. Figure 8 shows the equilibrium constant plot for reduction of NiO dissolved in an ideal solid solution. The standard state Gibbs energy data were obtained from JANAF table.[52] In the present experiment, dry hydrogen/argon gas mixture was used. The vapor pressure of H_2O is estimated as ~0.12 Pa in the flowing Ar condition according to Ref. [5]. The value of $\ln(P_{H_2}/P_{H_2O})$ is estimated to be ~10.64, which is a sufficient reductive atmosphere.

In our system, crystallization of mullite ahead of nickel was not preferred since mullite phase was not observed until the fibers were heat treated to 1400°C if the spinel phase precipitated first due to the presence of Ni^{2+}. At the same time, the α-Al_2O_3 phase was also observed as the secondary phase

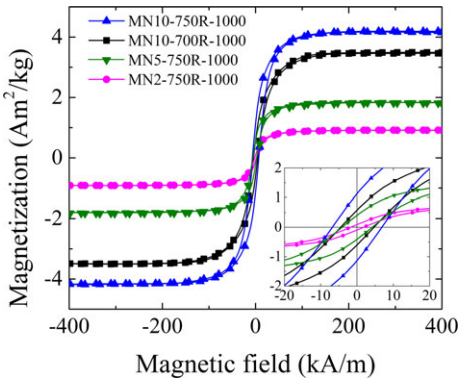

Fig. 7. Magnetic properties of mullite–nickel composite fibers.

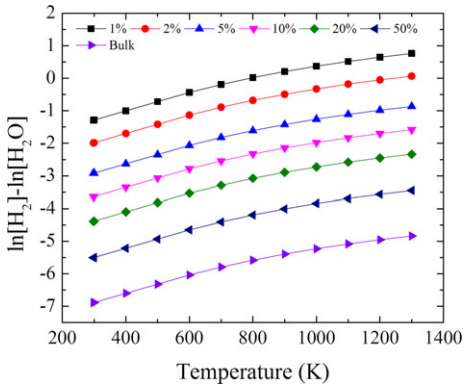

Fig. 8. Equilibrium constant plot for reduction of NiO dissolved in a solid solution (assuming ideal solution); the percentage indicates molar fraction of NiO in the solution.

(in Fig. 3). It was reported that the mullite phase was formed after crystallization of Al-Si spinel and reaction with amorphous silica induced by Ni^{2+}.[53] Complete reduction of Ni^{2+} ahead of mullization and spinel formation is necessary to obtain phase pure mullite.

(2) Crystallization of Matrix Phases

Depending on the homogeneity of the gel, sol–gel precursors are usually divided into monophasic and diphasic gels. The monophasic gel can be directly transformed to mullite phase without intermediate phases. The diphasic gel features the formation of intermediate phases, such as Al-Si spinel.[54] For the MN0 fibers, the monophasic gel characteristics were proven by XRD and DTA results showing no metastable phases during crystallization, which were also reported in our previous study.[40] For the fibers doped with nickel, the presence of Ni^{2+} cation induced the formation of spinel, which suppressed the formation of mullite until above 1400°C.[53]

If the fibers were isothermally reduced at a temperature lower than 750°C, spinel phase, instead of mullite, was formed at 1000°C. Table III summarizes the positions of the top three intense X-ray diffraction peaks which corresponded to 311, 400, and 440 crystalline planes of Al-Si and Ni-Al spinels. A systematic error up to 0.1° was assumed in our study due to the small uncertainty in sample height leveling and peak positioning (fitting). A clear trend can be seen with an increasing 2θ angle at higher isothermal reduction temperature, indicating a gradual decrease in lattice parameter.

In this study, the spinel phase identified could be a solid solution of Al-Si spinel and Al_2NiO_4 spinel. The Al_2NiO_4 spinel has a larger lattice parameter of 8.050 Å than those of Al-Si spinel.[55–57] In our experiment, more Ni^{2+} cations were converted into metallic phase at a higher reduction temperature. This coincided with our observation that the crystal unit cell became smaller if the fibers were reduced at higher temperatures. Therefore, we interpret that residual Ni^{2+} caused the formation of a solid solution Al-Si and Al-Ni spinels.

Upon thermal reduction, metallic nickel phase first nucleates within an amorphous Al_2O_3-SiO_2 matrix. After the Ni^{2+} cations were reduced, the Al_2O_3-SiO_2 matrix exhibited monophasic characteristics and crystallizes at around 950°C. This agrees well with our previous study, in which monophasic mullite devitrified at ~980°C.[40] The importance of retaining the monophasic characteristics is that a higher temperature (e.g., ~1400°C) for sintering is essentially needed to eliminate the spinel phase. This high-temperature heat treatment is undesirable because the metallic nickel NPs coarsens when the sintering temperature is close to the melting point of Ni (1455°C).[4] In that case it is susceptible to lose control over the size of nickel.

The mullization temperature in nickel–mullite systems reduced at 750°C is lower than that in nondoped mullite system as showed in DTA. This shift could be explained by the increasing number of sites available for nucleation-growth of mullite in the presence of finely dispersed nickel NPs. The boundary between Ni NPs and amorphous matrix tends to act as nucleation sites for mullite nucleation and growth.[58] The reduced energy barrier for nucleation can be used to explain this catalytic effect and temperature shift (about 30°C) for mullization.

The activation energies for crystallization of mullite and spinel phases can be calculated from DTA exothermic peaks at different heating rate using the Kissinger's equation[59]:

$$\ln\left(\frac{T_P^2}{P_r}\right) = \ln\left(\frac{E_a}{R}\right) + \frac{E_a}{RT_P} - \ln \nu \tag{4}$$

where T_p is the exothermic peak temperature, P_r is the heating rate, E_a is the activation energy for crystallization, R is the gas constant, and ν is the frequency factor constant.

Figure 9 shows the Kissinger's plot for peaks 1 to 3 in Fig. 4. This method has been reported to determine the activation energy for mullization by many authors.[60–62] The activation energies for mullization, spinel crystallization are summarized in Table IV. Okada showed that in monophasic gels, the E_a values for mullization ranged from 800 to 1400 kJ/mol.[62] The corresponding crystallization temperature had a maximum of about 1000°C.[62] We showed in our study that the pure mullite gel is monophasic. For mullization with the presence of Ni NPs, the activation energy was slightly smaller (1221 kJ/mol) than that in pure mullite gel. This difference could be assigned to the error generated in determining the T_p values of the broad exothermic peaks in mullite–nickel samples. Nevertheless, the value (1221 kJ/mol) stayed in the range for monophasic mullization. In Fig. 4, the DTA curve of MN5-H2 was significantly different from that of MN5-750R-H2, because in MN5-750R-H2, the pre-existing nickel nanoparticles served as heterogeneous nuclei for mullite growth. Under constant heating rate, heterogeneous nucleation and crystallization overlapped over a wide temperature range. Thus in the DTA curve of MN5-H2, instead of observing a strong exothermic peak, we did not observe an obvious peak. The activation energy for spinel formation in MN5-A specimen had been determined to be 1131 kJ/mol. This value was slightly lower than the diphasic mullite gel system doped with 3 wt% of nickel, of which has activation energy of 1320 kJ/mol was reported.[53]

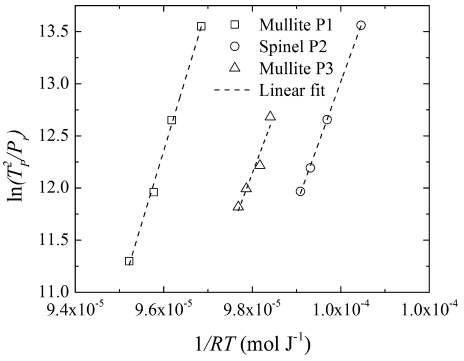

Fig. 9. Kissinger plots for crystallization peaks of P1, P2, and P3 in Fig. 4.

Table III. Comparison of the Peak Positions of {311}, {400}, and {440} of the Spinel Phase from This Work and References

	2θ (°)			
Specimen name	{311}	{400}	{440}	Reference
MN10-550R-1000	37.36	45.7	66.56	This work
MN10-650R-1000	37.36	45.7	66.65	This work
MN10-700R-1000	37.45	46.2	67.10	This work
Al_2NiO_4	37.01	45.0	65.55	[57]
Al-Si Spinel	37.81	46.0	66.65	[56]
γ-Al_2O_3	37.71	45.9	66.46	[56]

Table IV. Calculation of the Activation Energy and Avrami Constant for Nucleation and Growth of Ni–Mullite Fibers

	Mullization in MN0-A	Spinel crystallization in MN5-A	Mullization in MN5-750R
Activation energy (kJ/mol)	1403 ± 58	1131 ± 187	1221 ± 282
Avrami constant	3.156 ± 0.438	1.143 ± 0.063	0.773 ± 0.031

The crystallization mechanism could be determined from the Avrami constant n by the Augis–Bennett equation[63]:

$$n = \frac{2.5RT_P^2}{\Delta T E_a} \quad (5)$$

where ΔT is the full width at half maximum of the exothermic peak. Small value of n indicates surface crystallization mechanism instead of volume crystallization. The resulting Avrami constants are summarized in Table IV. A relatively greater value of n for mullite crystallization in MN0 specimen indicates a volume crystallization mechanism. This is attributed to the high mixing level and monophasic character of the gel. On the other hand, a small n for mullization in MN5 specimen was determined, revealing the surface crystallization mechanism. The surface crystallization mechanism was interpreted by the catalytic sites provided for nucleation at the nickel–glass interface that facilitates the growth.

(3) Magnetic Properties

Magnetic nanocomposites with large magnetic moment and low coercivity have been considered attractive for many applications.[64–66] The M_s, M_r, and H_c of bulk nickel at room temperature (300 K) are about 55 mAm^2/kg, 2.7 mAm^2/kg, and 8.0 kA/m.[67] The saturation magnetization of nanosized particles is usually smaller than that of the bulk materials due to the interfacial rearrangement of spins of ferromagnetic particles.[67–69] M_s of the composite fibers, if normalized by the weight of nickel, were about 70%–80% of the bulk nickel. It is known that coercivity of the magnetic particle is sensitive to the particle size corresponding to a single or multidomain structure. As the particle size decreases, fluctuations of the spin orientation become important and the particle behave as a superparamagnetic particle. The critical size of a single domain Ni particle, below which the ferromagnetic material exhibits superparamagnetic behavior, was reported in the range between 20 and 42 nm.[70–72] The small H_c observed in MN2-750R-1000 specimen indicated a stronger size effect. In our experiments, the normalized value M_r/M_s was about 0.1, the H_c of the 2% sample being 1.74 kA/m, implying the dominance of the superparamagnetic NPs. The suggested method to achieve superparamagnetism was to decrease the Ni concentration and lower the reduction temperature. A balance should be found between the desired magnetic properties and the resultant phases.

(4) Growth of Ni NPs

In the previous literature, precipitation and growth of metallic NPs in a refractory ceramics have been widely studied.[4,5,29] The growth of metallic NPs has been thought as a diffusion-limited process by the transport of either electrons or oxygen vacancies.[29] The Schmalzried model was applied to describe the growth of Ni NPs, which starts from the grain boundaries.[29, 73] In our work, we observed significantly different growth behaviors on the surface and within the ceramic host. The growth of the surface particles, which depended on the Ni concentration, was probably controlled by the diffusion process. As shown in Fig. 10, the NPs precipitated within mullite, on the other hand, were insensitive to the concentration of Ni, which indicates a totally different growth mechanism. It has been reported that the volume change during phase transformation can impose large strain energy on the system and thus possibly impose a thermodynamic energy well resulting in an equilibrium particle size.[74] We can hypothesize that similar theory can be applied to this phenomenon. The thermodynamics and kinetics of the particle growth will be elucidated in the future studies.

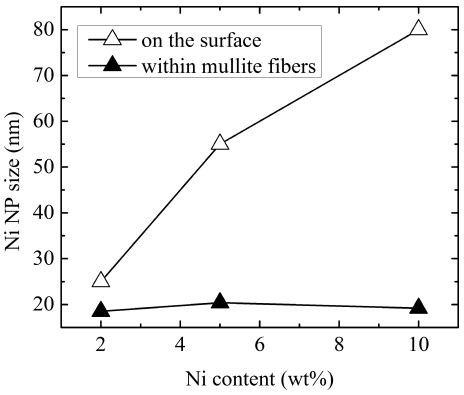

Fig. 10. The Ni NP sizes on the fiber surface and within mullite versus different Ni concentrations. The samples were heat treated at the same temperatures.

V. Summary

Mullite–nickel nanocomposite fibers were obtained via the reduction on heating the sol–gel/electrospinning-derived fibers. The reduction of the mullite–nickel fibers resulted in the nanocomposites with Ni NPs embedded in the mullite host fibers. With the reduction of Ni^{2+} at 750°C, the formation of spinel phase was prevented. Suppressing the spinel phase formation helped to obtain only mullite phase at low temperatures (~1000°C). Nickel NPs had a size of about 20 nm within the mullite fibers, which was insensitive to the Ni concentration. The growth of the Ni NPs on the fiber surfaces showed a typical diffusion-limited process. The surface Ni NPs had larger sizes with higher Ni concentration at the same heat-treatment temperatures. The presence of Ni NPs slightly lowered the temperature for mullization, which was ascribed to the catalytic effect of secondary phase particles providing heterogeneous nucleation growth sites at the interface between nickel NPs and matrix. The magnetic characterization of the composite fibers suggested ferromagnetism. A small coercivity close to superparamagnetic behavior was obtained in mullite fibers with Ni NPs, which was due to the small size of nickel NPs in the matrix. Relatively large Ni particles on the surface contributed to the ferromagnetism widening the hysteresis loop.

Acknowledgment

This project was funded by the Air Force Office of Scientific Research, Contract FA9550-12-1-0459. The authors would like to express their appreciation for the helpful suggestions and support of their contract monitor, Dr. Ali Sayir.

References

[1]T. Sekino and K. Niihara, "Microstructural Characteristics and Mechanical Properties for Al_2O_3/Metal Nanocomposities," *Nanostruct. Mater.*, **6** [5] 663–6 (1995).

[2]A. Das, M. Raffi, C. Megaridis, D. Fragouli, C. Innocenti, and A. Athanassiou, "Magnetite (Fe_3O_4)-Filled Carbon Nanofibers as Electro-Conducting/Superparamagnetic Nanohybrids and Their Multifunctional Polymer Composites," *J. Nanopart. Res.*, **17** [1] 1–14 (2015).

[3]R. Roy, "Ceramics by the Solution-Sol–Gel Route," *Science*, **238** [4834] 1664–9 (1987).

[4]H. Kondo, T. Sekino, N. Tanaka, T. Nakayama, T. Kusunose, and K. Niihara, "Mechanical and Magnetic Properties of Novel Yttria-Stabilized Tetragonal Zirconia/Ni Nanocomposite Prepared by the Modified Internal Reduction Method," *J. Am. Ceram. Soc.*, **88** [6] 1468–73 (2005).

[5]T. Sekino, T. Nakajima, S. Ueda, and K. Niihara, "Reduction and Sintering of a Nickel–Dispersed-Alumina Composite and Its Properties," *J. Am. Ceram. Soc.*, **80** [5] 1139–48 (1997).

[6]W. H. Tuan, H. H. Wu, and T. J. Yang, "The Preparation of AI_2O_3/Ni Composites by a Powder Coating Technique," *J. Mater. Sci.*, **30** [4] 855–9 (1995).

[7]J. S. Moya, S. Lopez-Esteban, and C. Pecharromán, "The Challenge of Ceramic/Metal Microcomposites and Nanocomposites," *Prog. Mater Sci.*, **52** [7] 1017–90 (2007).

[8]M. Nawa, T. Sekino, and K. Niihara, "Fabrication and Mechanical Behaviour of Al_2O_3/Mo Nanocomposites," *J. Mater. Sci.*, **29** [12] 3185–92 (1994).

[9]T. Ambrose, A. Gavrin, and C. L. Chien, "Formation and Magnetic Properties of Nanocomposite Fe-Al_2O_3 Using High-Energy Ball Milling," *J. Magn. Magn. Mater.*, **116** [3] L311–4 (1992).
[10]H. Takahashi, Y. Sunagawa, S. Myagmarjav, K. Yamamoto, N. Sato, and A. Muramatsu, "Reductive Deposition of Ni-Zn Nanoparticles Selectively on TiO_2 Fine Particles in the Liquid Phase," *Mater. Trans.*, **44** [11] 2414–6 (2003).
[11]E. Ramírez-Meneses, et al., "Preparation and Photocatalytic Activity of TiO_2 Films with Ni Nanoparticles," *J. Sol-Gel. Sci. Technol.*, **52** [2] 267–75 (2009).
[12]K. P. de Jong, "Synthesis of Supported Catalysts," *Curr. Opin. Solid State Mater. Sci.*, **4** [1] 55–62 (1999).
[13]M. Yoshinaga, H. Takahashi, K. Yamamoto, A. Muramatsu, and T. Morikawa, "Formation of Metallic Ni Nanoparticles on Titania Surfaces by Chemical Vapor Reductive Deposition Method," *J. Colloid Interface Sci.*, **309** [1] 149–54 (2007).
[14]T. Zhang, et al., "Mechanical Properties of Carbon Nanotube–Alumina Nanocomposites Synthesized by Chemical Vapor Deposition and Spark Plasma Sintering," *Composites Part A: Appl. Sci. Manuf.*, **40** [1] 86–93 (2009).
[15]R. G. Palgrave and I. P. Parkin, "Aerosol Assisted Chemical Vapor Deposition Using Nanoparticle Precursors: A Route to Nanocomposite Thin Films," *J. Am. Chem. Soc.*, **128** [5] 1587–97 (2006).
[16]J. M. Ballesteros, R. Serna, C. N. Afonso, A. K. Petford-Long, D. H. Osborne, and R. F. Haglund, "Pulsed Laser Deposition of Cu: Al_2O_3 Nanocrystal Thin Films with High Third-Order Optical Susceptibility," *Appl. Phys. Lett.*, **71** [17] 2445–7 (1997).
[17]J. P. Barnes, et al., "Structural Studies of Ag Nanocrystals Embedded in Amorphous Al_2O_3 Grown by Pulsed Laser Deposition," *Nanotechnology*, **13** [4] 465–70 (2002).
[18]N. M. Dempsey, et al., "Magnetic Behavior of Fe: Al_2O_3 Nanocomposite Films Produced by Pulsed Laser Deposition," *J. Appl. Phys.*, **90** [12] 6268–74 (2001).
[19]A. Santos, J. D. Ardisson, E. B. Tambourgi, and W. A. A. Macedo, "Synthesis of Granular $FeAl_2O_3$ by the Sol–Gel Method," *J. Magn. Magn. Mater.*, **177**, 247–8 (1998).
[20]E. D. Rodeghiero, O. K. Tse, J. Chisaki, and E. P. Giannelis, "Synthesis and Properties of Ni-α-Al_2O_3 Composites via Sol–Gel," *Mater. Sci. Eng.: A*, **195**, 151–61 (1995).
[21]H. Wang, T. Sekino, K. Niihara, and Z. Fu, "Preparation of Mullite-Based Iron Magnetic Nanocomposite Powders by Reduction of Solid Solution," *J. Mater. Sci.*, **44** [10] 2489–96 (2009).
[22]H. Kondo, et al., "Mechanical and Magnetic Properties of Nickel-Dispersed Tetragonal Zirconia Nanocomposites," *J. Nanosci. Nanotechnol.*, **2** [5] 485–90 (2002).
[23]T. Nakayama, et al., "Fabrication of MgO Based Nanocomposites with Multifunctionality," *J. Eur. Ceram. Soc.*, **24** [2] 259–64 (2004).
[24]S. Krompiec, J. Mrowiec-Białoń, K. Skutil, A. Dukowicz, L. Pająk, and A. B. Jarzębski, "Nickel–Alumina Composite Aerogel Catalysts with a High Nickel Load: A Novel Fast Sol–Gel Synthesis Procedure and Screening of Catalytic Properties," *J. Non-Cryst. Solids*, **315** [3] 297–303 (2003).
[25]J. Hernández-Torres and A. Mendoza-Galván, "Optical Properties of Sol–Gel SiO_2 Films Containing Nickel," *Thin Solid Films*, **472** [1] 130–5 (2005).
[26]Y. Liu, L. Zhang, Q. Guo, H. Hou, and T. You, "Enzyme-Free Ethanol Sensor Based on Electrospun Nickel Nanoparticle-Loaded Carbon Fiber Paste Electrode," *Anal. Chim. Acta*, **663** [2] 153–7 (2010).
[27]M. Awano, M. Sando, and K. Niihara, "Synthesis of Nanocomposite Ceramics for Magnetic Remote Sensing and Actuating," *Key Eng. Mater.*, **161**, 485–8 (1998).
[28]J. Jiang, Q. Gao, Z. Chen, J. Hu, and C. Wu, "Syntheses, Characterization and Properties of Novel Nanostructures Consisting of Ni/Titanate and Ni/Titania," *Mater. Lett.*, **60** [29] 3803–8 (2006).
[29]J. T. White, I. E. Reimanis, J. Tong, J. R. O'Brien, and A. Morrissey, "Internal Reduction of Ni^{2+} in ZrO_2 Stabilized with 10 mol% Y_2O_3 Examined with VSM and SQUID Magnetometry," *J. Am. Ceram. Soc.*, **95** [12] 4008–14 (2012).
[30]N. J. Tang, W. Zhong, W. Liu, H. Y. Jiang, X. L. Wu, and Y. W. Du, "Synthesis and Complex Permeability of Ni/SiO_2 Nanocomposite," *Nanotechnology*, **15** [12] 1756–8 (2004).
[31]I. A. Aksay, D. M. Dabbs, and M. Sarikaya, "Mullite for Structural, Electronic, and Optical Applications," *J. Am. Ceram. Soc.*, **74** [10] 2343–58 (1991).
[32]W. M. Kriven, et al., "High Temperature Single Crystal Properties of Mullite," *J. Eur. Ceram. Soc.*, **19** [13] 2529–41 (1999).
[33]P. C. Dokko, J. A. Pask, and K. S. Mazdiyasni, "High-Temperature Mechanical Properties of Mullite Under Compression," *J. Am. Ceram. Soc.*, **60** [3–4] 150–5 (1977).
[34]S. Kanzaki, H. Tabata, T. Kumazawa, and S. Ohta, "Sintering and Mechanical Properties of Stoichiometric Mullite," *J. Am. Ceram. Soc.*, **68** [1] C-6 (1985).
[35]K. K. Chawla, Z. R. Xu, and J. S. Ha, "Processing, Structure, and Properties of Mullite Fiber/Mullite Matrix Composites," *J. Eur. Ceram. Soc.*, **16** [2] 293–9 (1996).
[36]H. Schneider, J. Schreuer, and B. Hildmann, "Structure and Properties of Mullite—A Review," *J. Eur. Ceram. Soc.*, **28** [2] 329–44 (2008).
[37]G. B. Merrill and J. A. Morrison, "High Temperature Insulation for Ceramic Matrix Composites"; U.S. Patent No. 6,013,592. U.S. Patent and Trademark Office, Washington, DC, 2000.
[38]D. Li and Y. Xia, "Electrospinning of Nanofibers: Reinventing the Wheel?" *Adv. Mater.*, **16** [14] 1151–70 (2004).
[39]R. Ramaseshan, S. Sundarrajan, R. Jose, and S. Ramakrishna, "Nanostructured Ceramics by Electrospinning," *J. Appl. Phys.*, **102** [11] 111101, 17pp (2007).
[40]Z. Chen, et al., "Electrospun Mullite Fibers From the Sol–Gel Precursor," *J. Sol-Gel. Sci. Technol.*, **74** [1] 208–19 (2015).
[41]U. Selvaraj, S. Komarneni, and R. Roy, "Structural Differences in Mullite Xerogels from Different Precursors Characterized by ^{27}Al and ^{29}Si MASNMR," *J. Solid State Chem.*, **106** [1] 73–82 (1993).
[42]D. J. Cassidy, J. L. Woolfrey, J. R. Bartlett, and B. Ben-Nissan, "The Effect of Precursor Chemistry on the Crystallisation and Densification of Sol–Gel Derived Mullite Gels and Powders," *J. Sol-Gel. Sci. Technol.*, **10** [1] 19–30 (1997).
[43]T. Ban, S. Hayashi, A. Yasumori, and K. Okada, "Characterization of Low Temperature Mullitization," *J. Eur. Ceram. Soc.*, **16** [2] 127–32 (1996).
[44]V. Carles, C. Laurent, M. Brieu, and A. Rousset, "Synthesis and Characterization of Fe/Co/Ni Alloys-MgO Nanocomposite Powders," *J. Mater. Chem.*, **9** [4] 1003–9 (1999).
[45]A. H. Lu, E. E. Salabas, and F. Schüth, "Magnetic Nanoparticles: Synthesis, Protection, Functionalization, and Application," *Angew. Chem. Int. Ed.*, **46** [8] 1222–44 (2007).
[46]A. L. Patterson, "The Scherrer Formula for X-ray Particle Size Determination," *Phys. Rev.*, **56** [10] 978–82 (1939).
[47]B. D. Cullity, *Elements of X-ray Diffraction*, p. 101. Addison-Wesley, Reading, Massachusetts, 1978.
[48]K. Denbigh, *The Principles of Chemical Equilibrium*, p. 287. Cambridge University Press, Cambridge, 1966.
[49]S. Roy and D. Ganguli, "Optical Properties of Ni^{2+}-Doped Silica and Silicate Gel Monoliths," *J. Non-Cryst. Solids*, **151** [3] 203–8 (1992).
[50]V. V. Golubkov, et al., "The Influence of NiO on Phase Separation and Crystallization of Glasses of the MgO–Al_2O_3–SiO_2–TiO_2 System," *J. Non-Cryst. Solids*, **345**, 187–91 (2004).
[51]A. D. McNaught and A. D. McNaught, *Compendium of Chemical Terminology (Vol. 1669)*. Blackwell Science, Oxford.
[52]M. W. Chase, NIST-JANAF Thermochemical Tables. 1998.
[53]E. Tkalcec, S. Kurajica, and J. Schmauch, "Crystallization of Amorphous Al_2O_3–SiO_2 Precursors Doped with Nickel," *J. Non-Cryst. Solids*, **353** [30] 2837–44 (2007).
[54]L. S. Cividanes, T. M. Campos, L. A. Rodrigues, D. D. Brunelli, and G. P. Thim, "Review of Mullite Synthesis Routes by Sol–Gel Method," *J. Sol-Gel. Sci. Technol.*, **55** [1] 111–25 (2010).
[55]K. Okada and N. Ōtsuka, "Characterization of the Spinel Phase from Si O_2–Al_2O_3 Xerogels and the Formation Process of Mullite," *J. Am. Ceram. Soc.*, **69** [9] 652–6 (1986).
[56]G. W. Brindley and M. Nakahira, "The Kaolinite-Mullite Reaction Series: III, The High-Temperature Phases," *J. Am. Ceram. Soc.*, **42** [7] 319–24 (1959).
[57]C. O. Areán and J. D. Viñuela, "Structural Study of Copper-Nickel Aluminate ($Cu_xNi_{1-x}Al_2O_4$) Spinels," *J. Solid State Chem.*, **60** [1] 1–5 (1985).
[58]H. Choi-Yim and W. L. Johnson, "Bulk Metallic Glass Matrix Composites," *Appl. Phys. Lett.*, **71** [26] 3808–10 (1997).
[59]H. E. Kissinger, "Reaction Kinetics in Differential Thermal Analysis," *Anal. Chem.*, **29** [11] 1702–6 (1957).
[60]K. Okada, J. I. Kaneda, Y. Kameshima, A. Yasumori, and T. Takei, "Crystallization Kinetics of Mullite From Polymeric Al_2O_3–SiO_2 Xerogels," *Mater. Lett.*, **57** [21] 3155–9 (2003).
[61]A. Douy, "Crystallisation of Amorphous Spray-Dried Precursors in the Al_2O_3–SiO_2 System," *J. Eur. Ceram. Soc.*, **26** [8] 1447–54 (2006).
[62]K. Okada, "Activation Energy of Mullitization from Various Starting Materials," *J. Eur. Ceram. Soc.*, **28** [2] 377–82 (2008).
[63]J. Augis and J. Bennett, "Calculation of the Avrami Parameters for Heterogeneous Solid State Reactions Using a Modification of the Kissinger Method," *J. Thermal Anal.*, **13** [2] 283–92 (1978).
[64]S. Ohnuma, H. J. Lee, N. Kobayashi, H. Fujimori, and T. Masumoto, "Co-Zr-O Nano-Granular Thin Films With Improved High Frequency Soft Magnetic Properties," *Magnetics, IEEE Trans.*, **37** [4] 2251–4 (2001).
[65]S. E. Russek, et al., "High Frequency Measurements of CoFeHfO Thin Films," *Magnetics, IEEE Trans.*, **37** [4] 2248–50 (2001).
[66]S. Ohnuma and T. Masumoto, "High Frequency Magnetic Properties and GMR Effect of Nano-Granular Magnetic Thin Films," *Scripta Mater.*, **44** [8] 1309–13 (2001).
[67]J. H. Hwang, et al., "Magnetic Properties of Graphitically Encapsulated Nickel Nanocrystals," *J. Mater. Res.*, **12** [04] 1076–82 (1997).
[68]W. Wagner, A. Wiedenmann, W. Petry, A. Geibel, and H. Gleiter, "Magnetic Microstructure of Nanostructured Fe, Studied by Small Angle Neutron Scattering," *J. Mater. Res.*, **6** [11] 2305–11 (1991).
[69]J. J. Host, et al., "Effect of Annealing on the Structure and Magnetic Properties of Graphite Encapsulated Nickel and Cobalt Nanocrystals," *J. Appl. Phys.*, **83** [2] 793–801 (1998).
[70]C. Kittel, "Theory of the Structure of Ferromagnetic Domains in Films and Small Particles," *Phys. Rev.*, **70** [11–12] 965–71 (1946).
[71]W. Gong, H. Li, Z. Zhao, and J. Chen, "Ultrafine Particles of Fe, Co, and Ni Ferromagnetic Metals," *J. Appl. Phys.*, **69** [8] 5119–21 (1991).
[72]C. Estournes, T. Lutz, J. Happich, T. Quaranta, P. Wissler, and J. L. Guille, "Nickel Nanoparticles in Silica Gel: Preparation and Magnetic Properties," *J. Magn. Magn. Mater.*, **173** [1] 83–92 (1997).
[73]R. L. Everman and R. F. Cooper, "Internal Reduction of an Iron-Doped Magnesium Aluminosilicate Melt," *J. Am. Ceram. Soc.*, **86** [3] 487–94 (2003).
[74]S. J. Song, F. Liu, and Z. H. Zhang, "Analysis of Elastic–Plastic Accommodation Due to Volume Misfit Upon Solid-State Phase Transformation," *Acta Mater.*, **64**, 266–81 (2014). □